Inorganic Chemistry
Article
pubs.acs.org/IC

(Bis(terpyridine))copper(II) Tetraphenylborate: A Complex Example for the Jahn−Teller Effect

Andreas Meyer,[†] Gregor Schnakenburg,[‡] Robert Glaum,*[,‡] and Olav Schiemann*[,†]

[†]Institute of Physical and Theoretical Chemistry, University of Bonn, Wegelerstr. 12, Bonn, Germany
[‡]Institute of Inorganic Chemistry, University of Bonn, Gerhard-Domagk-Str. 1, Bonn, Germany

Supporting Information

ABSTRACT: The surprisingly complicated crystal structure of (bis(terpyridine))copper(II) tetraphenylborate $[Cu(tpy)_2](BPh_4)_2$ (tpy = 2,2′:6′,2″-terpyridine) consists of six crystallographically independent $[Cu(tpy)_2]^{2+}$ complexes. At ambient temperature, five out of six $[Cu^{II}N_6]$ chromophores appear to be compressed octahedra, while at 100 K, four exhibit elongated and only two compressed octahedral geometry. Temperature dependent single crystal UV/vis (100, 298 K) and EPR measurements (20, 100, 298 K) as well as AOM calculations suggest that the octahedra which show apparently compressed octahedral geometry (XRD) result from dynamic Jahn−Teller behavior of elongated octahedra $[Cu^{II}N_6]$. The detailed correlation of structural and spectroscopic data allows an understanding of the strongly solvent-dependent structures of the $[Cu(tpy)_2]^{2+}$ complex in solution.

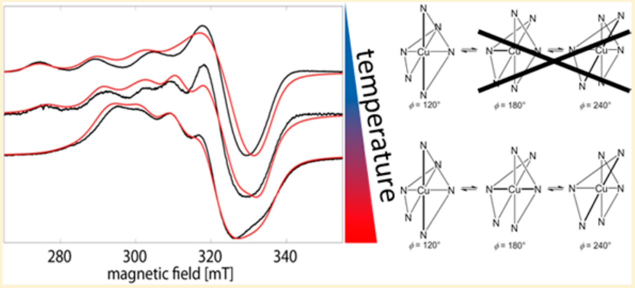

INTRODUCTION

Almost 80 years ago, Jahn and Teller showed that nonlinear, polyatomic systems in orbitally degenerate states are unstable with respect to nuclear displacements which lower the symmetry of the system.[1] The reason for this Jahn−Teller effect (JTE) is that the electron distribution is less symmetric than the nuclear distribution in such a situation and that the adiabatic approximation becomes invalid.[2,3] Extending the theory of the JTE to account for interactions of the ground state with excited states gives rise to the pseudo Jahn−Teller effect (PJTE).[4] The PJTE removes the restriction to nonlinear molecules and degenerate ground states imposed by Jahn and Teller. Recently, it was shown that the JTE and the PJTE are the only source of structural instability of polyatomic systems in their high symmetry configuration.[2,5] Therefore, the JTE and the PJTE have implications for virtually every chemical system that contains more than two atoms.[5] The reviews[2,3,5] by Bersuker give an up-to-date overview over both the JTE and the PJTE. While the occurrence of JTE or PJTE is not always appreciated in studies dealing with main group elements, its occurrence is more frequently discussed for transition metal complexes, e.g. in complexes of iron,[6−11] cobalt,[12,13] manganese,[14−16] and other metal ions.[17−20] Copper complexes are certainly the most widely studied JT active systems.[21−30] Experimentally, a major pitfall when studying JTE and PJTE system is the occurrence of dynamic effects.[31] As the JTE and the PJTE are brought about by vibrations, molecules in the regime of dynamic JTE or PJTE interconvert between different structures with the frequency of vibrations (i.e., interconversion frequencies in the terahertz range).[2,3,5] Such behavior leads to the observation of structures having an apparently higher symmetry than expected for JT-active systems using methods with time scales which are longer than the period of the molecular vibrations such as X-ray diffraction (usually several minutes) and EPR measurement (GHz regime).[31] The observation of electronic transitions on the other hand is expected to proceed much faster than molecular vibrations, and therefore electronic absorption spectroscopy should be able to reveal the true geometries of JT active complexes. While the experimental techniques to distinguish between dynamic and static JTE for crystalline samples have been developed by several researchers,[31−33] the investigation of solutions is more demanding.[34−36]

Here, we present the synthesis and temperature dependent X-ray crystallographic, EPR and UV/vis/NIR spectroscopic characterization of $[Cu(tpy)_2](BPh_4)_2$, **1**. The obtained detailed understanding of the correlation between structure and EPR properties will be applied to interpret the strongly solvent-dependent EPR behavior of the $[Cu(tpy)_2]^{2+}$ cation in solution.

EXPERIMENTAL SECTION

Synthesis. Methanol and DMSO (Sigma-Aldrich; chromatographical grade purity) have been used without further purification. Deuterated solvents for EPR (Deutero) and 2,2′:6′,2″-terpyridine (TCI Europe) were also used as bought. Metal salts have been purchased from Sigma-Aldrich.

Bis(2,2′:6′,2″-terpyridine)copper(II)bis(tetraphenylborate), **1**. A total of 80 mg (0.34 mmol) of 2,2′:6′,2″-terpyridine was dissolved in 6 mL of methanol, yielding a pale yellow solution. A total of 20 mg (0.15 mmol) of anhydrous copper dichloride dissolved in 3 mL of

Received: May 22, 2015
Published: August 14, 2015

DOI: 10.1021/acs.inorgchem.5b01157
Inorg. Chem. 2015, 54, 8456−8464

Table 1. Lattice Parameters of $[Cu(tpy)_2](BPh_4)_2$ at 100, 123, and 293 K

measurement	crystal	T/K	a/Å	b/Å	c/Å	β/deg
1	A	293(2)	40.278(3)	24.8878(17)	41.972(3)	116.277(2)
2	A	123(2)	40.001(2)	24.5857(2)	41.630(2)	116.319(2)
3	B	100(2)	39.9543(15)	24.5916(9)	41.6151(14)	116.252(2)

methanol were added to that solution, giving rise to an intensely colored green solution which was stirred at 50 °C for 5 min. A roughly 3-fold excess of sodium tetraphenylborate dissolved in methanol was then added, leading to the immediate precipitation of a green solid. The solvent was filtered off at 0 °C, and the remaining solid was washed three times with 4 mL of methanol at 0 °C. Drying under reduced pressure yielded **1** as a green powder. Crystals suitable for X-ray crystal structure determination were obtained from a saturated solution of **1** in DMSO, which was left overnight in an open vial (Yield: 90%). NMR: All ^1H resonances of the ligand have been broadened beyond recognition. The only remaining resonances at 7.16, 6.91, and 6.77 ppm are assigned to the tetraphenylborate anion. Anal. Calcd for **1**: C, 80.17, H 5.35, N 7.19. Found: C, 80.15; H, 5.25; N, 7.16. ESI-MS: 264.6 ($[Cu(tpy)_2]^{2+}$, 90%), 296.1($[Cu(tpy)]^+$, 100%), 365.2 ($[Na_2BPh_4]^+$, 55%).

X-ray diffraction. X-ray diffraction experiments with **1** have been conducted on two different crystals, A and B, at three different temperatures (Table 1). The monoclinic structure (space group $P2_1/c$) obtained using crystal B is in complete agreement with crystal A. In the temperature range from 100 to 293 K, no phase transition is observed in the XRD experiments, and the cell parameters vary only slightly with temperature (Table 1).

Intensity data were collected on a BRUKER X8-KappaApexII diffractometer using graphite monochromated Mo $K\alpha$ radiation (λ = 0.71073 Å). The diffractometer was equipped with a low-temperature device (Kryoflex, Bruker AXS GmbH, 100(2) K). Intensities were measured within 892 frames by fine-slicing ω and φ scans (rotational increment 0.5°; 60 s exposure time per frame) and corrected for background, polarization, and Lorentz effects. An empirical absorption correction was applied to the data set.[37] The structure was solved by direct methods and refined by the least-squares procedure implemented in the ShelX program system,[38] allowing for anisotropic displacement parameters. Hydrogen atoms were included isotropically using the riding model on the bound carbon atoms. CCDC 1061926−1061928 contain the supplementary crystallographic data for this paper, which can be obtained free of charge from The Cambridge Crystallographic Data Centre via www.ccdc.cam.ac.uk/data_request/cif. For further details, see the Supporting Information.

Single Crystal UV/vis/NIR Spectroscopy. A transparent dichroic crystal (blue/green; main crystal faces (001)/(00$\bar{1}$); approximate thickness d = 0.1 mm) was selected using an optical microscope and placed on the sample holder (aperture) using a small amount of grease. Polarized single crystal UV/vis/NIR spectra covering the spectral range from 5800 to 36 000 cm^{-1} have been recorded using a modified CARY 17 microcrystal spectrophotometer (spectral service, ANU Canberra, Australia). A halogen lamp was used as a light source. A photomultiplier (PMT) and a liquid nitrogen cooled Ge photodiode were used as detector systems for the UV and the visible region (11 111−36 000 cm^{-1}) and the NIR region (5800−16 666 cm^{-1}), respectively. For measurement in both spectral regions, the slit width was set to 0.08 mm. The reference intensities I_0 were measured with the same aperture, however, without the crystal. The spectra (Figure 3) show absorbance $A = -\log I/I_0$ vs wavenumber.

EPR Spectroscopy. EPR samples were prepared by filling 0.3 mL of 200 μM solutions of $[Cu(tpy)_2](BPh_4)_2$ in d_6-DMSO or mixtures of d_6-DMSO with either d_4-methanol or d_1-chloroform into quartz glass EPR tubes having an outer diameter of about 3.8 mm. The samples were then shock frozen using liquid nitrogen. For single crystal measurements, paper strips having a width of 1−2 mm were cut from a sheet of paper. A small amount of vacuum grease was put on one end of such a paper strip, which was used to mount the single crystals. Alignment of the crystals was achieved by visual inspection and controlled on EPR spectra obtained in preliminary experiments. For the powder measurements, single crystals have been carefully ground until a homogeneous powder was obtained. The homogeneity of these powders was evaluated by verifying the independence of the EPR spectrum from the sample orientation in the EPR spectrometer.

All EPR experiments were performed on a Bruker ELEXSYS E580 EPR spectrometer. A Super High-Q resonator and an Oxford ESR900 helium gas-flow cryostat were employed for cw measurements at X-band frequencies. For single crystal measurements, a programmable Bruker E 218-1001 goniometer was mounted on the SHQ resonator, allowing for free rotation around one axis. EPR measurements at Q-band frequencies were performed using an EN 5107D2 resonator and an Oxford CF935 helium gas-flow cryostat. Measurement parameters of the EPR experiments presented below are detailed in Tables S8−S10, S12, and S13 in the Supporting Information. Spectra were simulated using the "pepper" routine of the EasySpin program package.[39]

AOM Calculations. AOM calculations have been performed using the CAMMAG program.[40] The X-ray structures have been used as input geometries for the copper complexes. Only the first ligand sphere, i.e. the nitrogen donor atoms, has been considered. The e_σ parameter was set to 6800 cm^{-1} at a copper nitrogen distance d_0 = 2.00 Å. A radial dependence of $e_\sigma = 6800\ cm^{-1} \times (d_0/d)^{-5}$ has been assumed.[41] The ligand π interactions perpendicular to the plane of the ligands have been accounted for by using $e_\pi = 1/8e_\sigma$, while the in-plane π-interaction was assumed to be negligible. Configuration interaction between the metal 4s and 3d orbitals was included by introducing the parameter $e_{ds} = 0.15e_\sigma$ as discussed by Smith.[42] The orbital reduction factor k and the spin orbit coupling constant ζ were set to 0.8 and 664 cm^{-1}, respectively. The whole parametrization is in accordance with parameters used for describing similar systems.[41−45] Yet, the AOM parameters should not be overinterpreted in a physical sense, especially since a positive e_π paramater implies π-donating character, which is unusual for pyridine type ligands.

Choice of the Molecular Coordinate System. The molecular coordinate system has been chosen in accordance with the requirements imposed by group theory. Accordingly, the axis of highest symmetry is defined as the z axis.[46] Choosing the z axis in this way leads to an unusual denomination of the orbitals in some geometries described in the Results section as the axis of elongation and is not coinciding with the molecular z axis but is instead assigned to the molecular x axis. An elongated octahedron in such a coordinate system has a $y^2 - z^2$ SOMO and an x^2 HOMO in the one electron picture.[24] These orbitals have the same properties as the more conventional $x^2 - y^2$ and z^2 orbitals. A detailed discussion of the choice of the axis system is given in the Supporting Information.

■ RESULTS AND DISCUSSION

The synthesis of the tetraphenylborate of $Cu(tpy)_2^{2+}$ proceeds in a straightforward manner (Scheme 1). Mixing $CuCl_2$ and 2.2 equiv of tpy in methanol gives rise to intensely green colored solutions. Subsequent addition of an excess of sodium tetraphenylborate dissolved in methanol leads to immediate precipitation of $[Cu(tpy)_2](BPh_4)_2$ (**1**) as a green powder

Scheme 1. Synthesis of 1

$$CuCl_2 + 2\ tpy \xrightarrow{MeOH} [Cu(tpy)_2]Cl_2 \xrightarrow[-NaCl,\ MeOH]{xs\ NaBPh_4} [Cu(tpy)_2](BPh_4)_2$$

DOI: 10.1021/acs.inorgchem.5b01157
Inorg. Chem. 2015, 54, 8456−8464

which does not require any further purification after filtration and washing with methanol.

Interestingly, there have been publications on related copper(II) compounds which state that the obtained products or solutions are brown.[47−49] Our observations during the synthesis of **1** indicate that the brown color is a result of contamination with Cu^+ ions which stem either from impurities in the copper(II) salt used as a starting material or from partial reduction of copper(II) (for details, see the Supporting Information). Saturated DMSO solutions of **1** lead to crystallization of **1** as plate-like crystals with predominant faces (001) and $(00\bar{1})$. These crystals exhibit dichroic behavior (green/blue).

The crystal structure of **1** is typical[23,50−52] in the sense that the two tpy ligands are arranged for each Cu complex in a meridional fashion, thus giving rise to distorted octahedral coordination spheres (Figures 1 and 2). The angular strain within the ligand backbone pulls the outer N donors out of the equatorial plane leading to a D_{2d} symmetric structure. Complexes of this symmetry are subject to PJT distortions.[25]

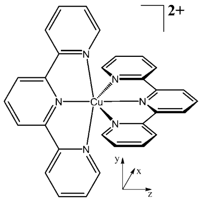

Figure 1. Schematic representation of the coordination structure of **1** with D_{2d} symmetry.

However, compared to other homoleptic copper complexes of 2,2′:6′,2″-terpyridine, the crystal structure of **1** is surprisingly complex with six independent $[Cu(tpy)_2]^{2+}$ cations in the asymmetric unit (Figure 2).[23,50−52] In all chromophores at all temperatures (100, 123, 293 K), the shortest distances d(Cu−N) (1.95−2.04 Å) are observed between copper and the central nitrogen atom of the two ligand molecules. It will be of importance for the explanation of the observed dichroic behavior that all these short interatomic vectors are aligned along the crystallographic a axis (Figure 2) with only small angular deviations. At ambient temperatures, five (**A**−**E**) out of the six chromophores $[Cu^{II}N_6]$ (Figure 2) appear to have compressed octahedral geometry very similar to the schematic D_{2d} symmetric coordination polyhedron in Figure 1 with four long distances d(Cu−N) ≈ 2.17 Å. Chromophore **F** (Figure 2) shows already at ambient temperature a slightly different distortion resembling an elongation, with two of the equatorial ligands at somewhat longer (d(Cu−N) = 2.19 and 2.25 Å) and the others at slightly shorter distances (d(Cu−N) = 2.09 and 2.09 Å). On cooling to 100 K, a very similar distortion pattern is assumed by chromophores **A**, **C**, and **E**, while **B** and **D** remain practically unchanged and the distortion of **F** approaches that of a typical 4 + 2 elongated octahedron.

Overall, the various $[Cu^{II}N_6]$ chromophores appear to change from D_{2d} symmetry with a 2 + 4 distance distribution at higher temperatures to C_{2v} symmetry and 4 + 2 distance distribution at lower temperatures. This change can be related to a temperature dependent competition between the strain trying to establish the optimum (undistorted) conformation of the ligand molecules and the forces trying to optimize the electronic energy of the coordinated cations. While at low temperatures, the electronic requirements of the Cu^{2+} ions (d^9 electron configuration) with their static Jahn−Teller effect are dominant. The occurrence of only a single elongated structure instead of two statistically disordered elongated octahedra is indicative of a cooperation between lattice forces and the JTE

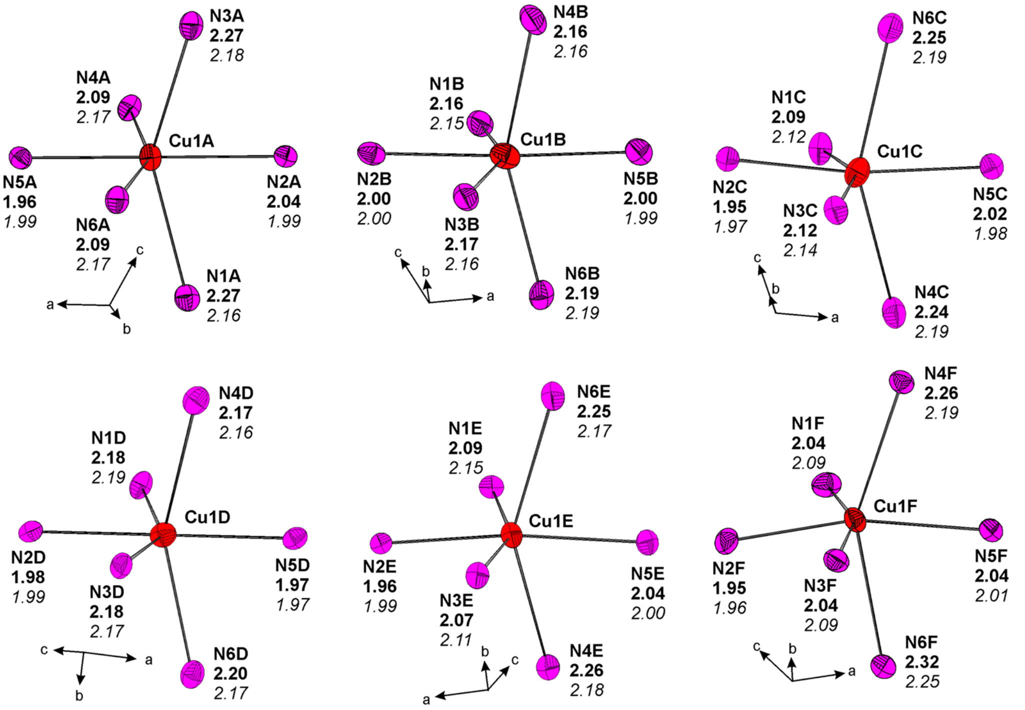

Figure 2. ORTEP style representation of the six crystallographically independent cations labeled **A**−**F** of $[Cu(tpy)_2](BPh_4)_2$ at T = 100 K. Ellipsoids at the 30% probability level, distances d(Cu−N) in Å at 100 K (bold); distances at 298 K (in *italics*). ESDs for distances are better than ±0.01 Å. Red ellipsoids represent Cu, and pink represent N atoms.

leading to one global minimum structure.[33] At ambient temperature, a dynamic JT behavior takes over. The apparently compressed structures observed using XRD experiments result from the averaging of the interconversion between two minimum structures. It appears to be noteworthy that the dynamic behavior of the various chromophores in the crystal structure of **1** is so different. Inspection of the crystal structure reveals that the cation anion separation as well as the cavity size of the cations appear to be no determinants of the different dynamic behavior. However, the static octahedra do show more C−H···π contacts between the complex cations and the anions than the compressed ones (16 contacts for the static octahedra compared to five contacts for the dynamic octahedra with a separation of less than 2.7 Å, see the Supporting Information for details). Similar observations have been made on iron complexes.[10,11]

Although conversion from elongated at low temperatures to apparently compressed octahedra at room temperature is typical for a transition from a static to a two-dimensional dynamic JT effect,[33] the XRD data alone are not fully conclusive. We have therefore applied temperature dependent UV/vis/NIR and EPR spectroscopy to corroborate the conclusions from the structural investigation.

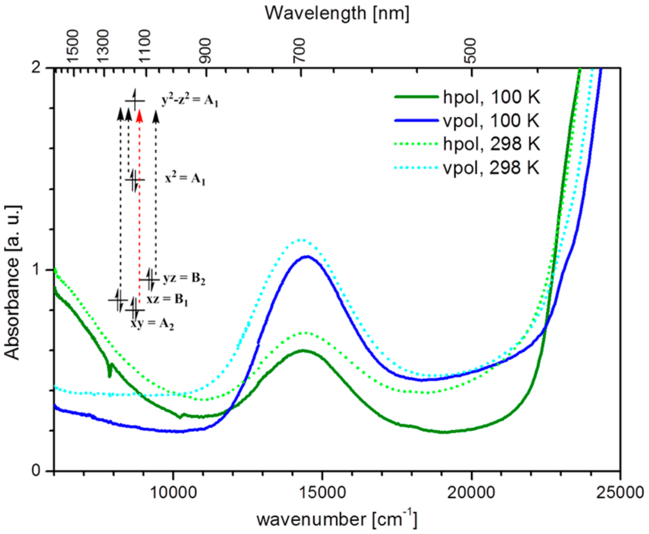

Figure 3. UV/vis/NIR spectra of a single crystal of **1** using polarized light. hpol = horizontally polarized light, vpol = vertically polarized light. Inset: d electron energy levels and allowed (black dotted arrows) and forbidden (red dotted arrows) transitions.

The single crystal UV/vis/NIR spectra (Figure 3) recorded at room temperature and 100 K show two broad absorption bands at $\tilde{\nu}_1 \approx 6000$ cm^{-1} and $\tilde{\nu}_2 \approx 14\,400$ cm^{-1} with pronounced polarization. The low energy transition allows estimation of a JT stabilization of $\tilde{\nu}_{JT} \approx (\tilde{\nu}_1/4) = 1500$ cm^{-1}.[23] The maximum of the band at 6000 cm^{-1} was confirmed by an additionally recorded powder reflectance spectrum (see Supporting Information, Figure S1). The high-energy absorptions at wavenumbers higher than 23 000 cm^{-1} are assigned to charge transfer transitions.[24] There is no significant difference in band intensities in the spectra recorded at ambient temperature and 100 K. This points to a static dipole mechanism for the d−d electronic transitions. Very clearly, the apparent changes in coordination geometry as deduced from the XRD study are not reflected by the UV/vis/NIR spectral behavior of the chromophores. In addition, it is quite unusual that a crystal structure containing six chemically similar, however crystallographically independent, chromophores exhibits dichroic behavior with strongly polarized bands. Typically, one would expect for such a situation averaging of orientation dependency in absorption properties. However, despite the complexity of the crystal structure of **1**, the two short Cu−N bonds of the central pyridine rings of each chromophore [$Cu^{II}N_6$] (the molecular *z* axis according to group theory; see Figure 1) are pointing almost parallel to the crystallographic *a* axis (Figure 2). The horizontal polarization (hpol) direction in our spectra is parallel to this axis. The vertical polarization (vpol) is aligned parallel to the crystallographic *b* axis. Assuming the selection rules for electronic excitation via a static dipole mechanism for an elongated octahedron [$Cu^{II}N_6$] of C_{2v} symmetry (C_2 parallel to the bond between Cu^{2+} and the nitrogen of the central pyridine rings) explains the observed polarizations: Excitation of an electron from x^2 to y^2−z^2 ($\tilde{\nu}_1 \approx 6000$ cm^{-1}; for orbital denomination see Figure 3) will occur only with light polarized along the short bonds Cu−N to the central pyridine rings (hpol). The electronic transitions *xz*, *yz* → y^2−z^2 ($\tilde{\nu}_2 \approx 14\,400$ cm^{-1}) can be excited by light polarized along the vpol direction (parallel to the crystallographic *b* axis). Since the octahedra are not perfectly aligned, the corresponding excitation will also occur (to a smaller extent) with light polarized along the crystallographic *a* axis (hpol).[46,53,54] Owing to the high time resolution of UV/vis/NIR spectroscopy, the electronic transitions of the elongated octahedra are observed for those cations, which are distorted by the dynamic JT effect and appear to be compressed in XRD experiments. Note also that the low energy transition would be forbidden along any polarization direction in a hypothetic, static, D_{2d} symmetrical compressed octahedral chromophore. Furthermore, since only two octahedra appear to be compressed at 100 K compared to five at 293 K, one would expect a marked decrease of the intensity of the low energy transition at higher temperatures if the compressed octahedra were indeed static. Yet, such an intensity change is also not observed. Conclusively, the polarized absorption spectra confirm the presence of elongated chromophores [$Cu^{II}N_6$] in **1** at 100 and 293 K but do not show signs of statically compressed octahedra, in agreement with the interpretation of the XRD data.

EPR spectra have been recorded at the temperatures of the UV/vis/NIR and XRD experiments. Furthermore, the experimental setup allowed extending the temperature range below 100 K. The spectra of the powder of **1** recorded at various temperatures at the X-band are shown in Figure 4.

Figure 4 shows how the relatively narrow four-line spectrum at room temperature is gradually converted into a broad four-line spectrum with the highest spectral density on the high field side at 20 K. In the intermediate temperature range a five line spectrum is observed, indicative of the simultaneous occurrence of apparently compressed and elongated octahedral complexes. Noteworthy, changes in the multiline pattern occur until the lowest temperature of 20 K.

Taking into account the results from the XRD experiments, this means that one octahedron is still static at room temperature while others appear to be dynamic down to temperatures as low as 40 K. Using 300 and 40 K as approximate transition temperatures and 400 cm^{-1} for the JT active vibration,[21] barrier heights of 250 cm^{-1} to more than 1800 cm^{-1} can be estimated for the interconversion between

DOI: 10.1021/acs.inorgchem.5b01157
Inorg. Chem. 2015, 54, 8456−8464

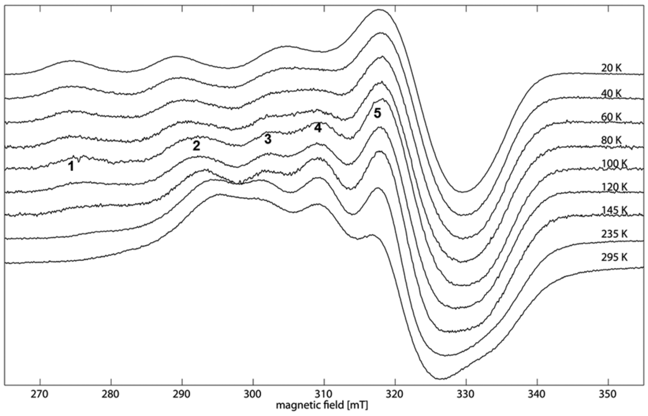

Figure 4. X-band EPR spectra of neat powdered **1** at various temperatures. The numbers **1**−**5** mark the five-line spectrum indicative of simultaneous occurrence of dynamic and static octahedra.

the two possible axes of elongation of the different cations observed crystallographically.[20] The lowest value for the cation which interacts the least with the surrounding lattice is in good agreement with values calculated for an isolated bis-(terpyridine)copper cation.[55] The highest barrier on the other hand is similar to the value obtained on a similar $[\mathrm{Cu^{II}N_6}]$ compound in which JT distortions have been reported.[24] It is noteworthy that the highest barrier is slightly higher than the estimated JT stabilization. This emphasizes the importance of the cooperative nature of lattice and JT forces.

In order to obtain more insight, the powder spectra obtained at room temperature, 100 K, and 20 K have also been recorded at Q-band frequencies and investigated more thouroughly. The spectra taken at room temperature show high spectral densities at their low field sides (295−330 and 1080−1130 mT, respectively. The shape of the EPR spectra corresponds to an inverse axial g tensor[31] for which $g_x = g_y > g_z$. Inverse axial g tensors are expected for compressed octahedra.[31] The shoulders at the low field sides of the spectra (285 and 1060 mT, respectively) are attributed to the elongated cation **F**. The spectra can be simulated best with the corresponding 5:1 ratio of compressed to elongated octahedra (Figure 5). At 100 K, the spectra can be simulated assuming four elongated and two effectively compressed octahedra (Figure 5). At 20 K, the X- and Q-band EPR spectra can be simulated assuming only static elongated octahedra (Figure 5).

In addition to the EPR experiments on the polycrystalline powder, single crystal EPR spectra have been recorded. The single crystal spectra could be simulated using the same set of parameters as for the powder spectra. As an example, the single crystal spectra taken at 100 K are shown in Figure 6 (the others are shown in the Supporting Information). Taking the complexity of the spectra into account, a satisfying agreement between experimental and simulated spectra is achieved at all orientations. Even for the crystal orientations shown in Figure 6c) where the EPR lines are heavily overlapping, the agreement of simulation and experiment is still acceptable. The parameters used to simulate the EPR spectra agree with the results of the AOM calculations (see Supporting Information). A noteworthy exception is the value of g_z for the apparently compressed octahedra, which was calculated to be nearly equal to the free electron g value, $g_e = 2.0023$. Experimentally, no g_z values lower than 2.04−2.05 have been observed which would be expected for elongated octahedra. This can be understood as an indication of the dynamic nature of the apparently compressed octahedra,[31] as the calculations were only performed with the average, seemingly compressed XRD structure (see Supporting Information).

It was possible to consistently simulate all EPR spectra and to theoretically validate the EPR parameters used in the simulations. Furthermore, the high quality of the XRD data obtained at 100 K provides a large body of structural information. Therefore, it should be possible to correlate the XRD structures with EPR parameters. Such a correlation requires knowledge of the distortion pathways of the $[\mathrm{Cu^{II}N_6}]$ cations and how these distortions affect the expected EPR parameters. To investigate the distortion pathways, the structural parameters obtained from the XRD experiment at 100 K are inspected. It is noted that the average bond lengths of the bonds along the z axis from the $\mathrm{Cu^{2+}}$ ion to the central pyridine rings of the tpy ligands $<d_z>$ as well as the bond lengths to the outer pyridine rings in the xy plane $<d_{xy}>$ are the same for all six cations **A**−**F**. They amount to $<d_z> = 1.993 \pm 0.009$ Å and $<d_{xy}> = 2.175 \pm 0.007$ Å. This finding suggests that removal of one ligand from the $\mathrm{Cu^{2+}}$ ion by a given distance leads to an equal approach of the other ligand.[56,57] For the ligand displacements Δd_{z+} and Δd_{z-} along the molecular z axis, it is found:

$$\Delta d_{z+} = -\Delta d_{z-} \tag{1}$$

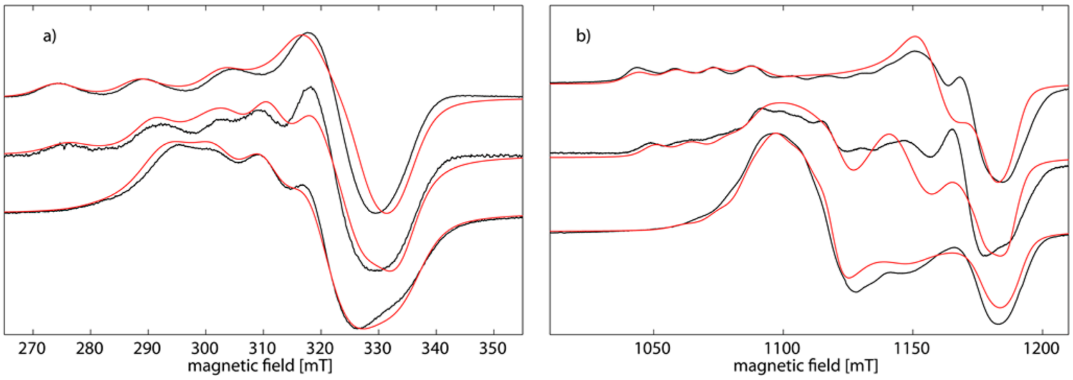

Figure 5. EPR spectra of neat powdered samples of **1** at different temperatures (from top to bottom T = 20, 100, and 293 K) and mw frequencies, (a) X-band and (b) Q-band. The black lines are the experimental data; the red lines are the corresponding simulations. The parameters used to simulate these spectra are given in Tables S5−S7.

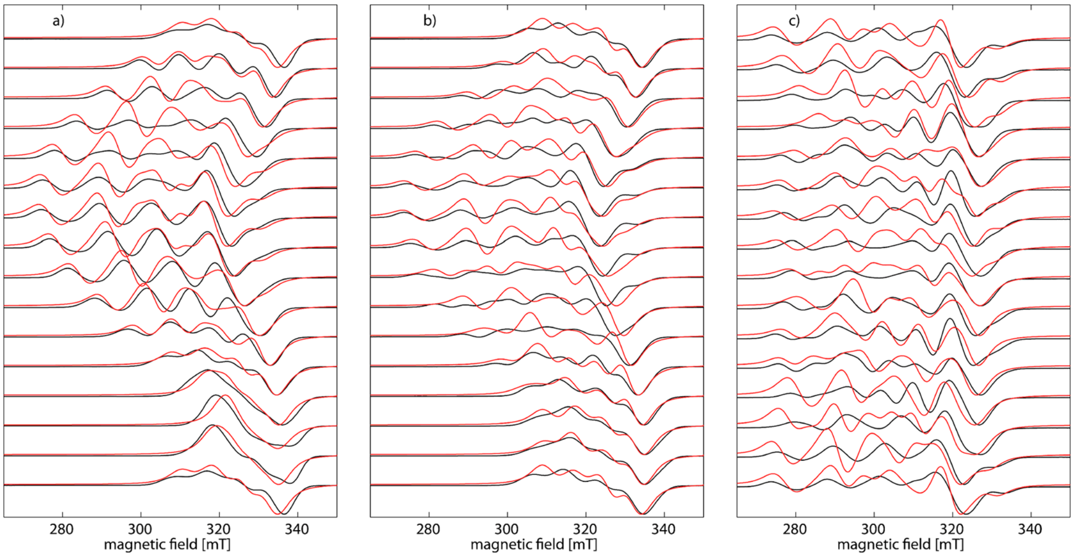

Figure 6. Single crystal EPR measurements at 100 K (black lines) and corresponding simulations thereof (red lines). (a) Rotation around crystallographic *b* axis. (b) Axis of rotation perpendicular to crystallographic *a* and *b* axes. (c) Rotation around the crystallographic *a* axis. See Supporting Information for single crystal spectrum taken at 20 K and room temperature.

Scheme 2. (a) Vector Model of the Displacement of the Nitrogen Donor Atoms[a] and (b) Interconversion of the Different Complex Conformers[b]

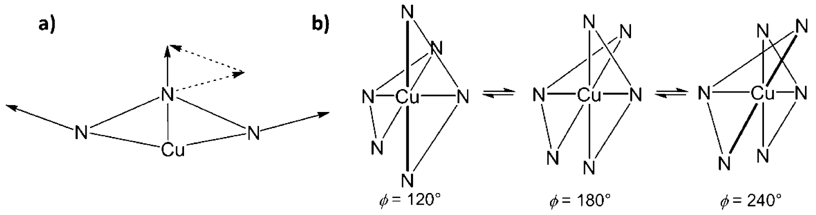

[a]The outer pyridine donor groups are displaced along their bond vectors. The displacement vector of the central pyridine ring is the sum of the displacement vectors of the outer pyridine rings. [b]The bold bonds indicate the unique axes.

In addition, if the central pyridine of one tpy ligand approaches the Cu^{2+} ion, the outer pyridine rings of that ligand do so as well and the other way round. However, the extent of the displacement of the outer rings is larger than for the central rings. If the x axis is chosen as the axis of elongation, inspection of the bond lengths observed in the crystal structure leads to the formulation of eq 2, which correlates the displacements[25,58−60] of the outer pyridine rings in the xy plane with Δd_{z+}:

$$\Delta d_x = -\Delta d_y = 2.38\Delta d_{z+} \qquad (2)$$

The ligand displacements Δd_x and Δd_y are the changes of the bond lengths Cu−N along the x and y axes, respectively, and are equal in magnitude but opposite in sign. The vibration described by the displacements Δd_x and Δd_y is the ε vibration in the JT E ⊗ e framework. However, the ε vibration does not contain a displacement of the ligands along the molecular z axis. Therefore, the displacement along the z axis must result from the rigid ligand structure, which forces the central pyridine ring to follow the movement of the outer pyridine rings. The correlation coefficient of 2.38 with a standard deviation of 0.29 is in agreement with a geometrical model of the ligand displacement if the outer pyridine rings are assumed to be displaced along their Cu−N bonds (Scheme 2a and Supporting Information for details). In the case of a D_{2d} symmetric compound, application of the PJT (A ⊕ B) ⊗ b framework might be considered more appropriate.[2,25] In this framework, the ligand displacement described above as ε vibration has b_1 symmetry, which is the expected symmetry within the PJT (A ⊕ B) ⊗ b framework.[2,25] The same conclusions are drawn in both frameworks and only the labeling of the vibration would change in the PJT framework. Here, the JT E ⊗ e framework is used to describe the ligand displacements as the JT radius ρ and angle ϕ introduced in this framework are used as descriptors of the geometry.

The displacements described by eqs 1 and 2 also suffice to illustrate the interconversion of an octahedron elongated along the x axis (JT angle of $\phi = 120°$) passing through a compressed state ($\phi = 180°$) over to a structure elongated along the y axis ($\phi = 240°$; Scheme 2b).

As all ligand displacements are correlated, a single displacement parameter suffices to describe all bond length parameters of the first ligand sphere. These bond length parameters can be correlated with the experimental EPR parameters using the equations given in the paper of Ammeter et al.[21] The g_x and g_y values react very sensitively to structural changes and can be reliably obtained from experimental data. The difference of these two values is expected to increase upon going from $\phi = 180°$ to $\phi = 120°$. A correlation of Δd_{z+} with $g_x - g_y$ for the six $[Cu^{II}N_6]$ ions at 100 K is shown in Figure 7.

These correlations between structure and EPR parameters gained on the solid state samples of **1** can now be applied to

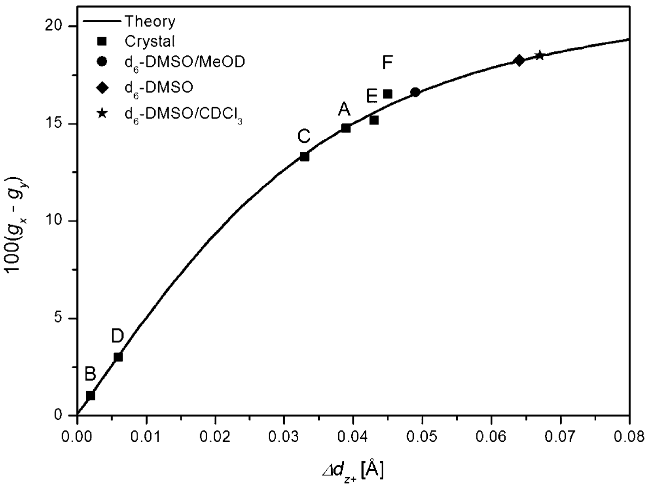

Figure 7. Correlation of Δd_{z+} with $g_x - g_y$ obtained from the EPR. The black line is the fit to the data points according to theoretical expectations.[21] **A**, **B**, **C**, **D**, **E**, and **F** are the six different $[\mathrm{Cu^{II}N_6}]$ ions in the crystal structure at 100 K. For frozen solutions, $g_x - g_y$ was obtained from simulation of the EPR spectra and subsequently used to infer the ligand displacement Δd_{z+} (see below).

gain insight about the structure of **1** in frozen solution. To that end, EPR samples of **1** dissolved in various solvent systems have been prepared and their EPR spectra at the X- and Q-bands have been recorded in order to evaluate the cation geometry depending upon the solvent. The results of these experiments are summed up in Figure 8.

The EPR spectra of solutions of **1** depend markedly on the choice of the solvent system. In polar solvents like d_6-DMSO or mixtures of d_6-DMSO/MeOD, a rhombic g tensor is observed ($g_x > g_y > g_z$). If a less polar solvent mixture like d_6-DMSO/CDCl$_3$ is used, an axial g tensor is observed ($g_x > g_y = g_z$). The nitrogen hyperfine coupling (HFC) structure displayed in the X-band EPR spectra of **1** dissolved in the solvent mixtures indicates that the Cu(II) ions are indeed ligated by six nitrogen donor atoms. Only in the case of pure d_6-DMSO could the nitrogen HFC structure not be resolved, as pure d_6-DMSO does not yield glassy samples. The obtained g and copper HFC values are given in Table S11 and lie within the bounds of those used to simulate the spectra of powdered or crystalline **1**. Assuming that the relation between geometric and EPR parameters is the same in solution and the solid state, one can calculate the geometric parameters for the complexes in solution with eqs 1 and 2, and the Δd_{z+} value can be read off from the graph in Figure 7. The obtained results are listed in Table 2.

According to Table 2, all cations found in frozen solution at 20 K correspond to elongated octahedra. However, the degree of distortion indicated by the JT radius ρ and the JT angle ϕ depends on the solvent. In the mixture of deuterated methanol and DMSO, the cation structure resembles those of the cations found in the crystal structure at 100 K, which still have a marked orthorhombic distortion as indicated by their JT angle $\phi \gtrsim 130°$. The other solutions contain cations that are closer to an ideal elongated structure along the x axis with JT angles ϕ close to 120° and JT radii > 0.38 Å. These values lie outside those observed crystallographically, which might indicate that the structural change is more complicated in d_6-DMSO and d_6-DMSO/CDCl$_3$ mixtures than just a more pronounced elongation. Therefore, the assignment of the structure in the case of the d_6-DMSO/MeOD solution has a higher degree of confidence than for the other solution. Further experiments on frozen solutions using for example MD simulations; EPR hyperfine spectroscopy; or EXAFS, XANES, and LAXS might be used to gain deeper insight into the structures in different solutions.

Note that the theoretical treatment also yields expressions for the SOMO and the HOMO.[21] Both these orbitals have antibonding character. For all observed elongated structures, the HOMO in this framework has nearly pure x^2 character. This means that only very weak bonding forces and therefore very elastic bonds between the Cu^{2+} ion and the outer pyridine rings of the remote tpy ligand are expected.[61] Thus, the remote ligand is activated for ligand displacement.[35]

■ CONCLUSION

The tetraphenylborate of the (bis(terpyridine))copper(II) complex **1** crystallizes in a remarkably complicated structure. The crystal structure revealed the existence of six crystallographically independent complex cations with highly variable bond lengths of $d_x \approx 2.175{-}2.300$ Å, $d_y \approx 2.045{-}2.175$ Å, and $d_z \approx 1.955{-}2.045$ Å, and each of these cations shows different dynamic behavior. In addition to the X-ray experiments, UV/vis/NIR and EPR spectroscopy have been applied to investigate the behavior of the different complex cations. The intensity of the electronic transitions at 6000 and 14 400 cm^{-1} was used to confirm the dynamic nature of the apparently compressed octahedra. The low-energy transition can be used to estimate a JT stabilization of 1500 cm^{-1}. In EPR spectroscopically, the g

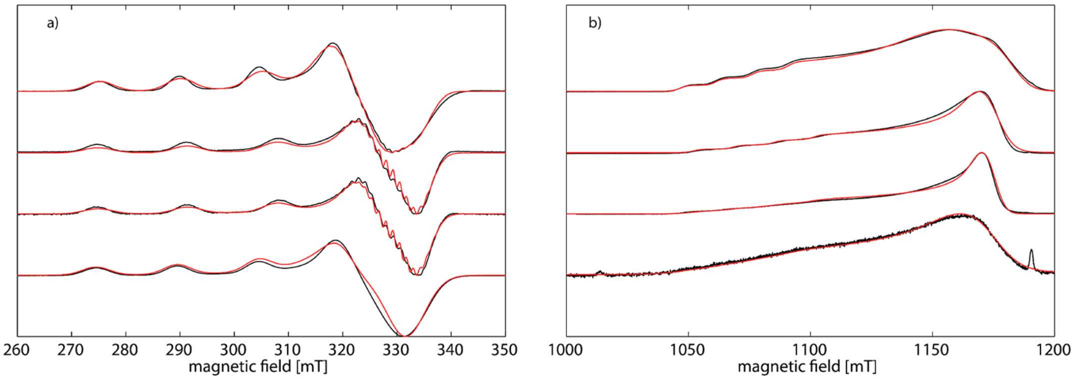

Figure 8. Spectra of frozen solutions of **1** at (a) X- (b) and Q-band frequencies in d_6-DMSO, d_6-DMSO/CDCl$_3$ (1:3), DMSO/CDCl$_3$ (1:5), and d_6-DMSO/MeOD (1:1.5) (from bottom to top). T = 20 K. Black: experimental spectra. Red: simulated spectra.

Table 2. Geometrical Parameters of $[Cu(tpy)_2]^{2+}$ Inferred from EPR Spectra of Frozen Solutions of **1**[a]

solvent	$100 \cdot \Delta g_{xy}$	Δd_{z+}/Å	d_{z+}/Å	d_{z-}/Å	d_x/Å	d_y/Å	ρ/Å	ϕ/deg
d_6-DMSO	18.25	0.064	2.057	1.929	2.327	2.023	0.381	123.9
d_6-DMSO/MeOD	16.6	0.049	2.042	1.944	2.292	2.058	0.322	130.8
d_6-DMSO/$CDCl_3$[b]	18.5	0.067	2.060	1.926	2.334	2.016	0.402	122.3

[a]The bond lengths have been calculated using $d_{z+} = <d_z> + \Delta d_{z+}$, $d_{z-} = <d_z> + \Delta d_{z-}$, $d_x = <d_{xy}> + \Delta d_x$ and $d_y = <d_{xy}> + \Delta d_y$ [b]The EPR parameters are the same for both mixtures of d_6-DMSO and $CDCl_3$ (1:3 and 1:5).

values have been correlated with the structures of the cations. The g values amount to $g_x \approx 2.260$, $g_y \approx 2.110$, and $g_z \approx 2.045$ for static elongated octahedra and to $g_x \approx 2.185 \approx g_y$ and $g_z \approx 2.045$ of the apparently compressed octahedra, where the g_z value of the latter is another indication of the dynamic nature of the cations. The experimental results have been analyzed using the angular overlap model. To account for the dynamic behavior of the cations, their potential energy surface has to be assumed to contain two minima corresponding to elongation along the molecular x and y axes, respectively. The hypothetic compressed structure lies on the saddle point in between the two minima, which is also the energetic barrier for interconversion of the two elongated isomers. For those cations that reach the dynamic JT at lower temperatures, the energy barrier between the two minima has to be smaller than for those that reach the dynamic JT at higher temperature. The energy barrier can be estimated to lie between 250 and 1800 cm^{-1}. The different barrier heights may be explained by secondary cation contacts.

In addition, experiments on frozen solutions revealed that the structure of the cations is also affected by the solvent matrix. Since the EPR parameters of the Cu^{2+} ion react very sensitively on even slight changes of the bonding parameters of the ligating atoms, it was possible to infer details concerning the structure of the first coordination sphere, assuming that the description of the complex as a $[Cu^{II}N_6]$ octahedron is still valid. In order to obtain a deeper understanding of the origin of the different dynamic behaviors of the $[Cu^{II}N_6]$ octahedra, quantum chemical and further experiments on solutions are ongoing.

■ ASSOCIATED CONTENT

Ⓢ Supporting Information

The Supporting Information is available free of charge on the ACS Publications website at DOI: 10.1021/acs.inorgchem.5b01157.

> Simulation parameters and simulations of single crystal EPR spectra, UV/vis/NIR spectra of the neat powdered **1**, UV/vis/NIR spectra of solutions of **1**, and a discussion of the color of **1** (PDF)

■ AUTHOR INFORMATION

Corresponding Authors

*E-mail: rglaum@uni-bonn.de.
*E-mail: schiemann@pc.uni-bonn.de.

Notes

The authors declare no competing financial interest.

■ ACKNOWLEDGMENTS

We thank V. Dittrich for performing the UV/vis/NIR measurements and Prof. Dr. A. Filippou for access to his X-ray diffractometers. O.S. and R.G. thank the DFG for funding via SFB 813.

■ REFERENCES

(1) Jahn, H. A.; Teller, E. *Proc. R. Soc. London, Ser. A* **1937**, *161*, 220−235.

(2) Bersuker, I. B. *The Jahn-Teller Effect*; Cambridge University Press: New York, 2006.

(3) Bersuker, I. B. *Chem. Rev.* **2001**, *101*, 1067−1114.

(4) Fulton, R. L.; Gouterman, M. *J. Chem. Phys.* **1961**, *35*, 1059−1071.

(5) Bersuker, I. B. *Chem. Rev.* **2013**, *113*, 1351−1390.

(6) Constable, E. C.; Baum, G.; Bill, E.; Dyson, R.; van Eldik, R.; Fenske, D.; Kaderli, S.; Morris, D.; Neubrand, A.; Neuburger, M.; Smith, D. R.; Wieghardt, K.; Zehnder, M.; Zuberbühler, A. D. *Chem. - Eur. J.* **1999**, *5*, 498−508.

(7) Zhang, X.; Lawson Daku, M. L.; Zhang, J.; Suarez-Alcantara, K.; Jennings, G.; Kurtz, C. A.; Canton, S. E. *J. Phys. Chem. C* **2015**, *119*, 3312−3321.

(8) Kershaw Cook, L. J.; Thorp-Greenwood, F. L.; Comyn, T. P.; Cespedes, O.; Chastanet, G.; Halcrow, M. A. *Inorg. Chem.* **2015**, *54*, 6319−6330.

(9) Nihei, M.; Shiga, T.; Maeda, Y.; Oshio, H. *Coord. Chem. Rev.* **2007**, *251*, 2606−2621.

(10) Hasegawa, Y.; Sakamoto, R.; Takahashi, K.; Nishihara, H. *Inorg. Chem.* **2013**, *52*, 1658−1665.

(11) Vela, S.; Novoa, J. J.; Ribas-Arino, J. *Phys. Chem. Chem. Phys.* **2014**, *16*, 27012−27024.

(12) Ramakrishna, B.; Salzer, A.; Ruppli, U.; Ammeter, J.; Kölle, U. *Inorg. Chem.* **1986**, *25*, 1364−1368.

(13) Waizump, K.; Takuno, M.; Fukushima, N.; Masuda, H. *J. Coord. Chem.* **1998**, *44*, 269−279.

(14) Barra, A.; Gatteschi, D.; Sessoli, R.; Abbati, G. L.; Cornia, A.; Fabretti, A. C.; Uytterhoeven, M. G. *Angew. Chem., Int. Ed. Engl.* **1997**, *36*, 2329−2331.

(15) Hargittai, M.; Réffy, B.; Kolonits, M.; Marsden, C. J.; Heully, J.-L. *J. Am. Chem. Soc.* **1997**, *119*, 9042−9048.

(16) Romain, S.; Duboc, C.; Neese, F.; Rivière, E.; Hanton, L. R.; Blackman, A. G.; Philouze, C.; Leprêtre, J.; Deronzier, A.; Collomb, M. *Chem. - Eur. J.* **2009**, *15*, 980−988.

(17) Bruyndonckx, R.; Daul, C.; Manoharan, P.; Deiss, E. *Inorg. Chem.* **1997**, *36*, 4251−4256.

(18) Khomenko, V.; Langer, K.; Rager, H.; Fett, A. *Phys. Chem. Miner.* **1998**, *25*, 338−346.

(19) Thauern, H.; Glaum, R. *Inorg. Chem.* **2007**, *46*, 2057−2066.

(20) Barriuso, M. T.; Ortiz-Sevilla, B.; Aramburu, J. A.; García-Fernández, P.; García-Lastra, J. M.; Moreno, M. *Inorg. Chem.* **2013**, *52*, 9338−9348.

(21) Ammeter, J.; Bürgi, H.; Gamp, E.; Meyer-Sandrin, V.; Jensen, W. *Inorg. Chem.* **1979**, *18*, 733−750.

(22) Comba, P.; Kerscher, M. *Cryst. Eng.* **2003**, *6*, 197−211.

(23) Folgado, J. V.; Henke, W.; Allmann, R.; Stratemeier, H.; Beltran-Porter, D.; Rojo, T.; Reinen, D. *Inorg. Chem.* **1990**, *29*, 2035−2042.

(24) Mack, K.; Wünsche von Leupoldt, A.; Förster, C.; Ezhevskaya, M.; Hinderberger, D.; Klinkhammer, K. W.; Heinze, K. *Inorg. Chem.* **2012**, *51*, 7851−7858.

(25) Murphy, B.; Hathaway, B. *Coord. Chem. Rev.* **2003**, *243*, 237−262.

(26) Bacci, M. *Chem. Phys.* **1986**, *104*, 191−199.

(27) Simmons, C. J.; Hathaway, B. J.; Amornjarusiri, K.; Santarsiero, B. D.; Clearfield, A. *J. Am. Chem. Soc.* **1987**, *109*, 1947−1958.

(28) Simmons, C. J.; Hitchman, M. A.; Stratemeier, H.; Schultz, A. J. *J. Am. Chem. Soc.* **1993**, *115*, 11304−11311.

(29) Docherty, R.; Tuna, F.; Kilner, C. A.; McInnes, E. J.; Halcrow, M. A. *Chem. Commun.* **2012**, *48*, 4055−4057.

(30) Hitchman, M. A.; Maaskant, W.; van der Plas, J.; Simmons, C. J.; Stratemeier, H. *J. Am. Chem. Soc.* **1999**, *121*, 1488−1501.

(31) Halcrow, M. A. *Dalton Trans.* **2003**, 4375−4384.

(32) Murphy, B.; Hathaway, B. *Coord. Chem. Rev.* **2003**, *243*, 237−262.

(33) Falvello, L. *J. Chem. Soc., Dalton Trans.* **1997**, 4463−4476.

(34) Persson, I.; Persson, P.; Sandström, M.; Ullström, A.-S. *J. Chem. Soc., Dalton Trans.* **2002**, 1256−1265.

(35) Schwenk, C. F.; Rode, B. M. *ChemPhysChem* **2003**, *4*, 931−943.

(36) Chaboy, J.; Muñoz-Páez, A.; Merkling, P. J.; Marcos, E. S. *J. Chem. Phys.* **2006**, *124*, 064509.

(37) *SADABS*; Bruker AXS Inc.: Billerica, MA, 2001.

(38) Sheldrick, G. *Acta Crystallogr., Sect. A: Found. Crystallogr.* **2008**, *64*, 112−122.

(39) Stoll, S.; Schweiger, A. *J. Magn. Reson.* **2006**, *178*, 42−55.

(40) Cruse, D. A.; Davies, J. E.; Gerloch, M.; Harding, J. H.; Mackey, D. J.; McMeeking, R. F. *CAMMAG, A FORTRAN Computing Package*; University Chemical Laboratory, Cambridge, England, 1979.

(41) McDonald, R. G.; Hitchman, M. A. *Inorg. Chem.* **1990**, *29*, 3074−3080.

(42) Smith, D. W. *Inorg. Chim. Acta* **1977**, *22*, 107−110.

(43) Astley, T.; Canty, A. J.; Hitchman, M. A.; Rowbottom, G. L.; Skelton, B. W.; White, A. H. *J. Chem. Soc., Dalton Trans.* **1991**, 1981−1990.

(44) Astley, T.; Gulbis, J. M.; Hitchman, M. A.; Tiekink, E. R. T. *J. Chem. Soc., Dalton Trans.* **1993**, 509−515.

(45) Astley, T.; Ellis, P. J.; Freeman, H. C.; Hitchman, M. A.; Keene, F. R.; Tiekink, E. R. *J. Chem. Soc., Dalton Trans.* **1995**, 595−601.

(46) Harris, D. C.; Bertolucci, M. D. *Symmetry and Spectroscopy*; Dover Publications Inc.: Mineola, NY, 1989.

(47) Narr, E.; Zimmermann, H.; Godt, A.; Goldfarb, D.; Jeschke, G. *Phys. Chem. Chem. Phys.* **2003**, *5*, 3959−3967.

(48) Hoover, J. M.; Ryland, B. L.; Stahl, S. S. *J. Am. Chem. Soc.* **2013**, *135* (6), 2357−2367.

(49) De Bruin, B.; Bill, E.; Bothe, E.; Weyhermüller, T.; Wieghardt, K. *Inorg. Chem.* **2000**, *39*, 2936−2947.

(50) Allmann, R.; Henke, W.; Reinen, D. *Inorg. Chem.* **1978**, *17*, 378−382.

(51) Valdes-Martinez, J.; Toscano, R. A.; Salazar-Mendoza, D. *Acta Crystallogr., Sect. E: Struct. Rep. Online* **2001**, *57*, m331−m332.

(52) Hitchman, M. A.; Yablokov, Y. V.; Petrashen, V. E.; Augustyniak-Jabłokov, M. A.; Stratemeier, H.; Riley, M. J.; Łukaszewicz, K.; Tomaszewski, P. E.; Pietraszko, A. *Inorg. Chem.* **2002**, *41*, 229−238.

(53) Cotton, F. A. *Chemical Applications of Group Theory*; Wiley-Interscience, 1989.

(54) Hitchman, M. A.; Riley, M. J.; Solomon, E. I.; Lever, A. B. P. *Inorganic Electronic Structure and Spectroscopy*; Wiley-Interscience: New York.

(55) Deeth, R. J.; Hearnshaw, L. J. A. *Dalton Trans.* **2006**, 1092−1100.

(56) Comba, P.; Okon, N.; Remenyi, R. *J. Comput. Chem.* **1999**, *20*, 781−785.

(57) Bürgi, H. B.; Dunitz, J. D. In *Structure Correlation*; Wiley-VCH Verlag GmbH: Weinheim, Germany, 1994; pp 163−204.

(58) Comba, P. *Coord. Chem. Rev.* **1999**, *185−186*, 81−98.

(59) Der Heyde, T. A. *Angew. Chem., Int. Ed. Engl.* **1994**, *33*, 823−839.

(60) Murphy, G.; Nagle, P.; Murphy, B.; Hathaway, B. *J. Chem. Soc., Dalton Trans.* **1997**, 2645−2652.

(61) Comba, P.; Schiek, W. *Coord. Chem. Rev.* **2003**, *238−239*, 21−29.